Supporting Information: Photochemical Transformation of Weakly Absorbing Organics by Visible Light in Microdroplets

Alexander Logozzo,[1] and Thomas C. Preston*[1,2]

1. Department of Chemistry, McGill University, Montreal, Quebec, Canada

2. Department of Atmospheric and Oceanic Sciences, McGill University, Montreal, Quebec, Canada

* Thomas C. Preston

e-mail: thomas.preston@mcgill.ca

Contents

1 Parameters for Determining Concentration

Table S1 lists the physicochemical constants that are used to determine the time-dependent solute concentration $c_{\mathrm{A}}(t)$ from precise refractive index measurements.

Partial specific volumes $\bar{\mathrm{v}}$ for water, glycine, proline, and serine come from the CRC Handbook.[S1] For glucose, $\bar{\mathrm{v}}$ was obtained by extrapolating CRC aqueous-solution density data to the density of the pure solute.[S1] For ribose and deoxyribose, $\bar{\mathrm{v}}$ was assigned the representative organic value $1/1500\ \mathrm{m^3\,kg^{-1}}$.[S2]

The hygroscopicity parameter κ for glycine and serine was calculated from activity coefficients generated with AIOMFAC[S3,S4] at the experimental relative humidity (RH). The proline value was taken directly from Ref. S5. For glucose, κ was derived at the experimental RH using the activity parameterizations in Ref. S6. For ribose and deoxyribose, the same approach was applied using the activity parameterizations in Ref. S7.

The molecular polarizability α for water was obtained from the refractive index of pure water at $\lambda = 589$ nm ($n = 1.333$) via the Clausius–Mossotti relation for a neat liquid. For all solutes, α was determined by extrapolating refractive index measurements to $t = 0$, applying the Clausius–Mossotti relation for a single-solute aqueous solution, and estimating the composition with κ–Köhler theory at the experimental RH. The uncertainties given for α correspond to the one standard deviation obtained by applying this procedure to several droplets of the same solute.

Table S1: Physicochemical parameters used in the concentration–retrieval model. Molar mass M, partial specific volume $\bar{\mathrm{v}}$, hygroscopicity parameter κ, and molecular polarizability α at $\lambda = 589$ nm for each molecule are listed.

Molecule	M ($\mathrm{kg\,mol^{-1}}$)	$\bar{\mathrm{v}}$ ($10^{-4}\,\mathrm{m^3\,kg^{-1}}$)	κ	α ($10^{-40}\,\mathrm{m^3\,molecule^{-1}}$)
Water	0.01802	10.028	–	0.337
Glycine	0.07507	5.754	0.536	1.98±0.03
Proline	0.11513	7.189	0.420	3.46±0.04
Serine	0.10509	5.769	0.226	2.51±0.02
Glucose	0.18016	6.551	0.207	4.67±0.10
Ribose	0.15013	6.667	0.244	4.09±0.04
Deoxyribose	0.13413	6.667	0.336	3.64±0.02

2 Photokinetic Fit Parameters

Table S2 summarizes the parameters obtained by fitting the time-dependent concentration measurements in Figures 2 and 3 of the main article. Equation 2 was fitted with the parameters β and t_0 constrained by Equation 3, so that the sole adjustable parameters are the ratio ϕ_2/ϕ_1 and the product $\sigma_A\phi_2$. Those two quantities were obtained by simultaneously applying a nonlinear least-squares fit to every droplet-size data set for each solute. A constant incident photon flux of $\Phi = 1.191\times10^{18}$ photons s^{-1} was used in all calculations.

Table S2: Parameters of best-fit for ϕ_2/ϕ_1 and $\sigma_A\phi_2$ in Equations 3.

Molecule	ϕ_2/ϕ_1 (M^{-1})	$\sigma_A\phi_2$ ($m^2\,M^{-1}$)
Glycine	4.98×10^{1}	6.07×10^{-34}
Proline	3.67×10^{1}	6.30×10^{-33}
Serine	1.38×10^{1}	4.37×10^{-33}
Glucose	2.51×10^{2}	1.01×10^{-33}
Ribose	2.28×10^{1}	2.08×10^{-33}
Deoxyribose	1.09×10^{1}	1.22×10^{-33}

3 Reference Single-Particle Measurements with Non-volatile and Volatile Solutes

As part of the validation of the photochemical analysis in the main text, we examined two non-reactive droplets as reference points. Figure S1 shows an aqueous droplet that contains a non-volatile solute (LiCl). During the 10^5 s experiment the radius and the refractive index at 589 nm remain constant within experimental uncertainty, aside from changing due to fluctuations in the cell RH. Figure S2 shows an aqueous droplet of the volatile solute 1,2,6-hexanetriol. In this case, the radius decreases steadily over 1.2×10^4 s while the refractive index remains constant. This behaviour is characteristic of solute evaporation accompanied by water loss (the composition stays fixed as the droplet maintains equilibrium with the surrounding RH).

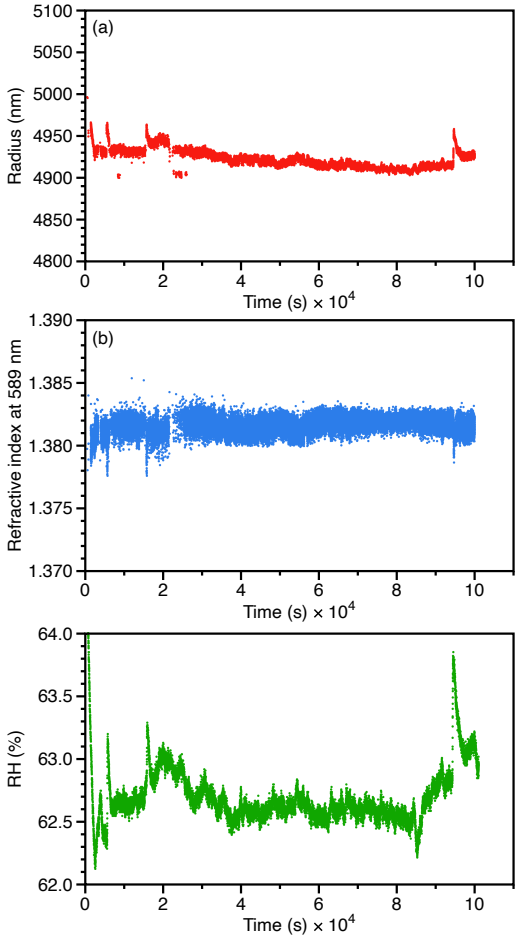

Figure S1: Single-particle measurement for an aqueous LiCl droplet held at fixed RH for 100,000 s. Measured (a) radius, (b) refractive index at 589 nm, and (c) RH as a function of time. The droplet was trapped with a 532 nm laser with a power set to 800 mW.

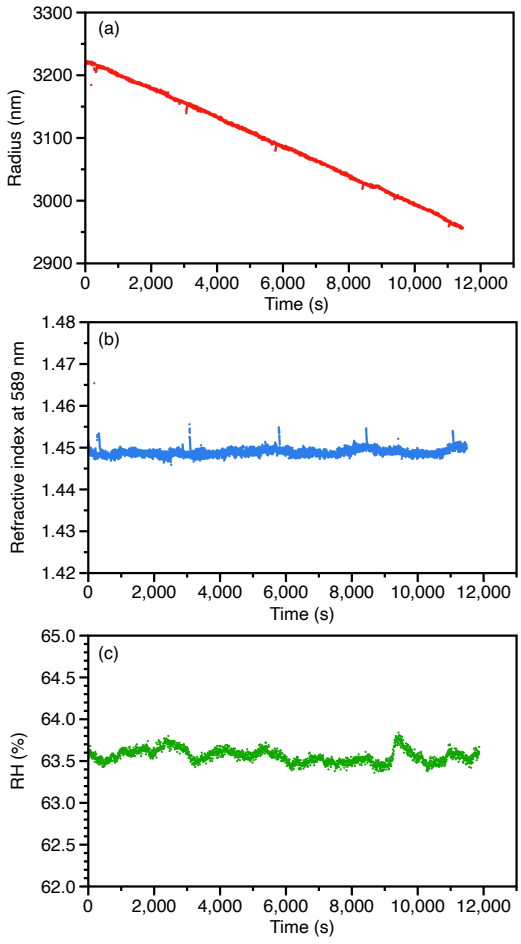

Figure S2: Single-particle measurement for an aqueous 1,2,6-hexanetriol droplet held at fixed RH for 12,000 s. Measured (a) radius, (b) refractive index at 589 nm, and (c) RH as a function of time. The droplet was trapped with a 532 nm laser with a power set to 200 mW.

4 Raman Spectra of Trapped Droplets

Figures S3 and S4 compare spontaneous Raman spectra collected at the start of each experiment ($t = 0$) and at the end of the trapping lifetime (which is roughly $t = t_0$). Morphology-dependent resonances (MDRs) have been removed so that vibrational bands and changes in the broadband OH stretch are clearly visible. For aqueous amino-acid droplets (Figure S3) and sugar droplets (Figure S4), a pronounced decrease in OH-stretch intensity confirms net water loss, while new bands or band-shape changes indicate formation of photoproducts. All measurements were performed with 532 nm excitation at either 300 mW or 400 mW under the RHs stated in each panel.

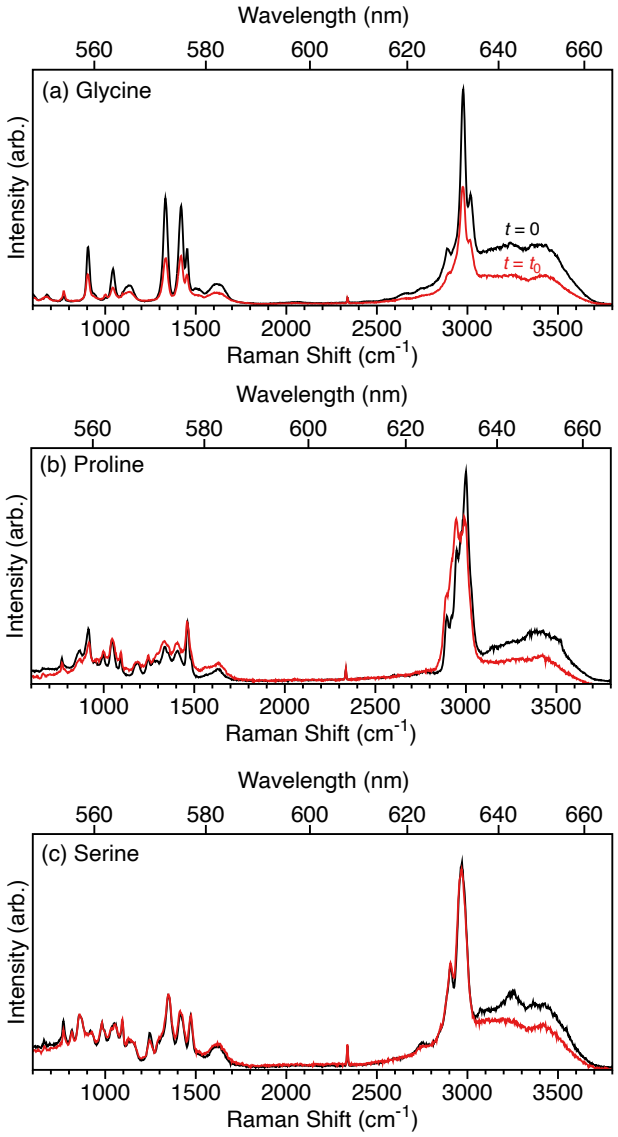

Figure S3: Spontaneous Raman spectra with MDRs removed for aqueous (a) glycine, (b) proline, and (c) serine droplets. Spectra recorded at $t = 0$ are shown in black and those recorded at the trapping lifetime ($t \approx t_0$) are shown in red. RHs were (a) 63±1%, (b) 67±1%, and (c) 67±1%. Excitation wavelength was 532 nm and laser powers were (a) 400 mW, (b) 300 mW, and (c) 300 mW.

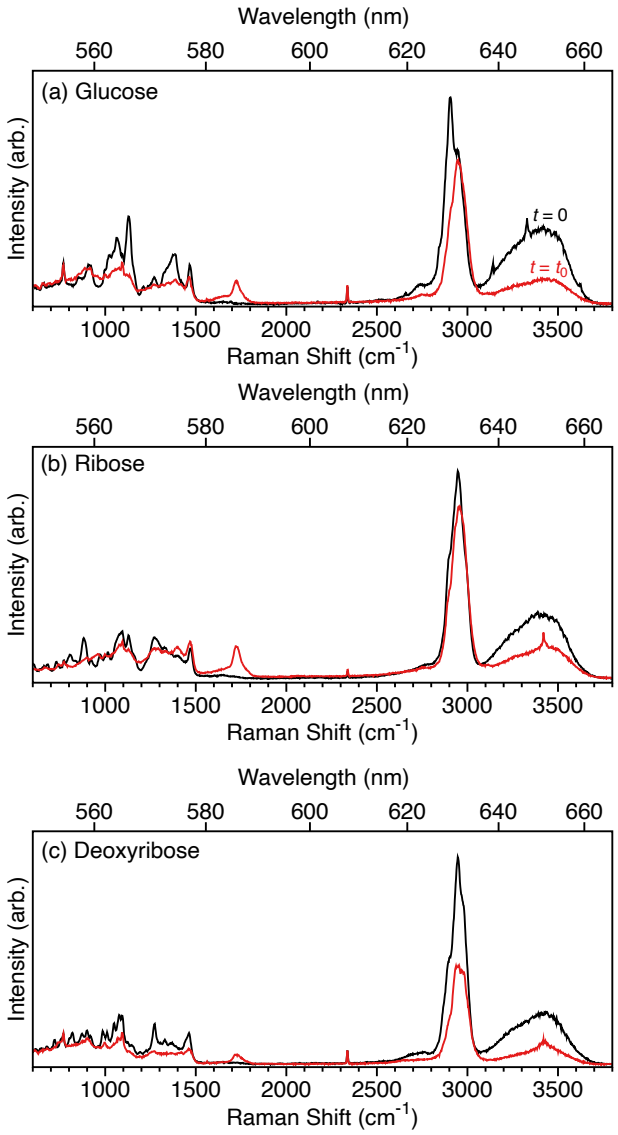

Figure S4: Spontaneous Raman spectra with MDRs removed for aqueous (a) glucose, (b) ribose, and (c) deoxyribose droplets. Spectra recorded at $t = 0$ are shown in black and those recorded at the trapping lifetime ($t \approx t_0$) are shown in red. RHs were (a) 65±1%, (b) 64±1%, and (c) 64±1%. Excitation wavelength was 532 nm and laser powers were (a) 400 mW, (b) 300 mW, and (c) 300 mW.

5 Time-Dependent Raman Intensity and Refractive Index from Single Droplets

Figure S5 contrasts two approaches for tracking reaction progress: integrating the product Raman band versus determining the refractive index from MDRs. Photoproduct formation in all three aqueous sugar droplets is monitored by integrating the carbonyl stretch band at 1720±30 cm^{-1}, a spectral region free of parent-sugar features that reflects the growth of the newly formed C=O group (see Figure S4). Because a comparably distinct photoproduct band is absent in the amino-acid droplets (Figure S3), no analogous comparison is presented for those systems. The peaks that appear throughout the measurements in the left column of Figure S5 arise from MDRs that sweep across the carbonyl stretch band as droplet size and composition change over time. This moving interference is superimposed on the true product signal, making quantitative concentration determination by Raman band integration impractical.

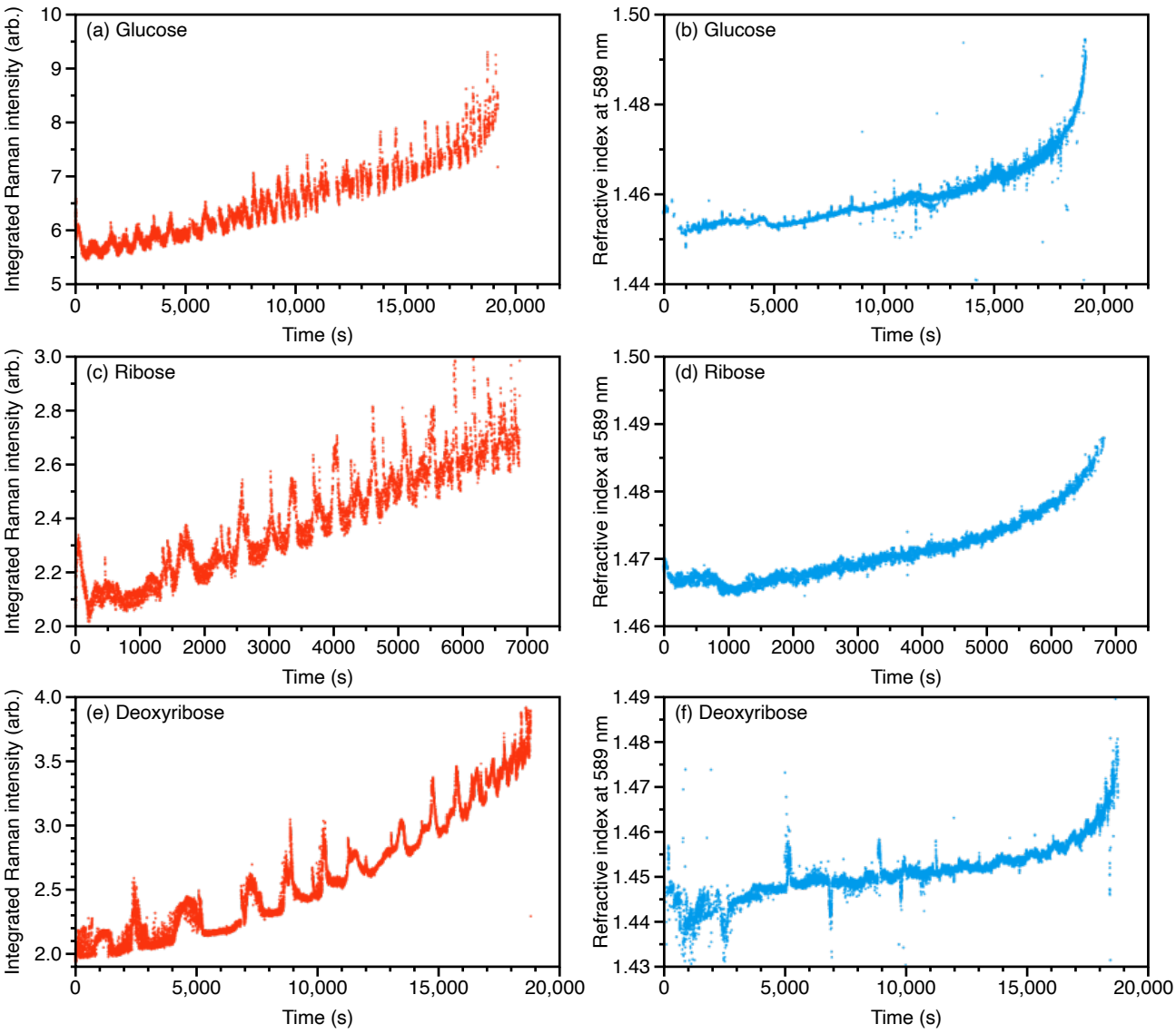

Figure S5: Integrated Raman intensity of the carbonyl product band (left column) and refractive index at 589 nm obtained from MRFIT for the same droplets (right column) as a function of time for aqueous solutions of (a,b) glucose, (c,d) ribose, and (e,f) deoxyribose. The RH during the experiments was 74±1% for glucose, 66±1% for ribose, and 67±1% for deoxyribose. All measurements were performed using a $\lambda = 473$ nm laser at 500 mW.

6 Effect of Dissolved Oxygen on Droplet Photochemistry

To investigate whether indirect oxidation by ozone or oxygen-derived radicals contributes to the observed photochemistry, we compared the evolution of identically prepared proline droplets held in purified air and in purified nitrogen. As shown in Figure S6, the radius and refractive index profiles are nearly indistinguishable under the two carrier gases, and the trapping lifetimes are identical within experimental error. The absence of any change in droplet shrinkage or refractive index increase under air indicates that dissolved oxygen does not play a significant role in the observed photochemistry.

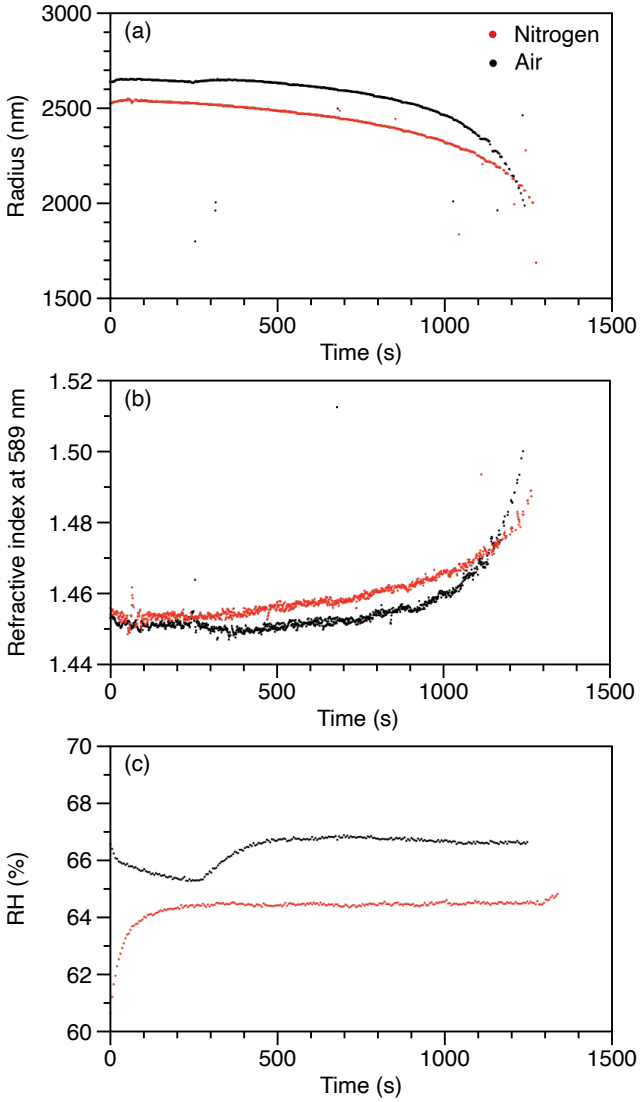

Figure S6: Influence of carrier-gas composition on a single aqueous proline droplet. (a) Radius and (b) refractive index at 589 nm, extracted from MDR fitting, are shown as functions of time for the same nominal RH when the flow cell is purged with nitrogen (red) or air (black). (c) Measured RH during each experiment. All measurements were performed using a $\lambda = 473$ nm laser at 500 mW.

7 Coupled-Dipole Model and Effective Medium Model Calculations for Aqueous Organic Solutes

7.1 Polarizability Model

We used a simplified model of molecular polarizability to investigate how molecules interact with each other in response to an applied electromagnetic field. For the organic species studied here, the lowest energy UV electronic transitions are approximated using a single Lorentz oscillator. Specifically, the complex and wavelength-dependent microscopic polarizability, α_d, of each molecule in a vacuum is modeled using a single Lorentzian function[S8]

$$\alpha_d(\lambda) = \alpha_\infty + \frac{\alpha_1 \lambda_1}{\mu_1} \left(\frac{1}{1 - \frac{\lambda_1^2}{\lambda^2} - i\frac{\lambda_1^2}{\lambda \mu_1}} - 1 \right), \tag{S1}$$

where λ is the vacuum wavelength of light, α_∞ is the static polarizability of the molecule (the polarizability as $\lambda \to \infty$), and, for the electronic transition being represented, α_1 is the oscillator strength, μ_1 the full width at half-maximum, and λ_1 is the resonance wavelength.

DFT calculations were performed with Gaussian 16 and GaussView 6 to optimize the molecular geometries, compute the static polarizability, and to calculate the molar absorption coefficients.[S9,S10] For static polarizability geometries and calculations the PBE0[S11] hybrid functional, the def2-TZVP[S12,S13] basis set, and a polarizable continuum model (PCM)[S14,S15] were employed. This methodology has been shown to reproduce the static polarizability of Rhodamine 6G with sufficient accuracy to permit subsequent determination of its wavelength-dependent polarizability.[S16] Static polarizabilities for all solutes are given in Table S3.

For the amino acids (glycine, proline, and serine), the parameters α_1, μ_1, and λ_1 were fitted to far-ultraviolet (FUV) molar absorptivity measurements from Ref. S17. Figure S7a–c compares these experimental spectra with the single-oscillator Lorentzian fits. For the sugars (glucose, ribose, and deoxyribose), FUV molar absorptivity measurements were not available, so the parameters were obtained by fitting time-dependent DFT (TD-DFT) spectra. The CAM-B3LYP[S18] functional, the aug-cc-pVDZ[S19] or aug-cc-pVTZ (glycine) basis set, and PCM[S14,S15] solvation were used. As shown in Figure S7, the TD-DFT calculations satisfactorily reproduce the amino acid spectra and should therefore provide reasonable estimates for the sugars.

Implicit solvation was used to calculate absorption spectra due to its low computational cost and satisfactory agreement with measured molar absorption coefficients upon benchmarking. Štěpánek and Bouř showed that explicit solvation from molecular dynamics trajectories offered better predictions of absorption spectra for zwitterionic amino acids,[S20] but the intensity of experimental spectra was not reproduced.[S21] All panels of Figure S7 compare the TD-DFT spectra with the corresponding single-oscillator fits.

The Lorentz oscillator model used in Equation S1 is known to overpredict absorption in the low-energy (long wavelength) tails of electronic transitions.[S16] To assess the impact of this limitation, we also considered a Voigt-type description of the lineshape, which provides a more accurate representation of the low-energy tails,[S16] by modeling the microscopic polarizability using a Pseudo-Voigt profile. The Pseudo-Voigt form approximates the Voigt lineshape by combining Lorentzian and Gaussian character through a weighted sum rather than a full convolution. The Pseudo-Voigt polarizability for a single transition can be written as

$$\alpha_d^{\mathrm{PV}}(\lambda) = \alpha_\infty + f\cdot\frac{\alpha_1\lambda_1}{\mu_1}\left(\frac{1}{1-\frac{\lambda_1^2}{\lambda^2}-i\frac{\lambda_1^2}{\lambda\mu_1}}-1\right)+(1-f)\cdot\frac{\alpha_1\lambda_1}{\mu_1}\exp\left[-\frac{(\lambda-\lambda_1)^2}{2\sigma_1^2}\right]\left(i\frac{\mu_1}{\lambda_1}-1\right), \quad \text{(S2)}$$

where σ_1 is related to μ_1 and λ_1 by

$$\sigma_1 = \frac{\lambda_1^2}{2\mu_1\sqrt{2\ln 2}}, \quad \text{(S3)}$$

and f is the fraction parameter ($0 \leq f \leq 1$) controlling the Lorentzian character. The fraction parameter $f = 1$ recovers the pure Lorentzian profile of Equation S1, while $f = 0$ gives a pure Gaussian profile. This Pseudo-Voigt approach provides a computationally efficient way to model intermediate lineshapes and assess the sensitivity of our analysis to deviations from the pure Lorentzian assumption. In Figure S7, the Pseudo-Voigt model is compared with the single Lorentz oscillator.

Additionally, Figure S8 compares the TD-DFT FUV molar absorptivity spectra of the six solutes investigated here with that of dicyandiamide (DCD). Consistent with its much faster photochemical reactivity, DCD exhibits a markedly stronger FUV absorption band than the other species.

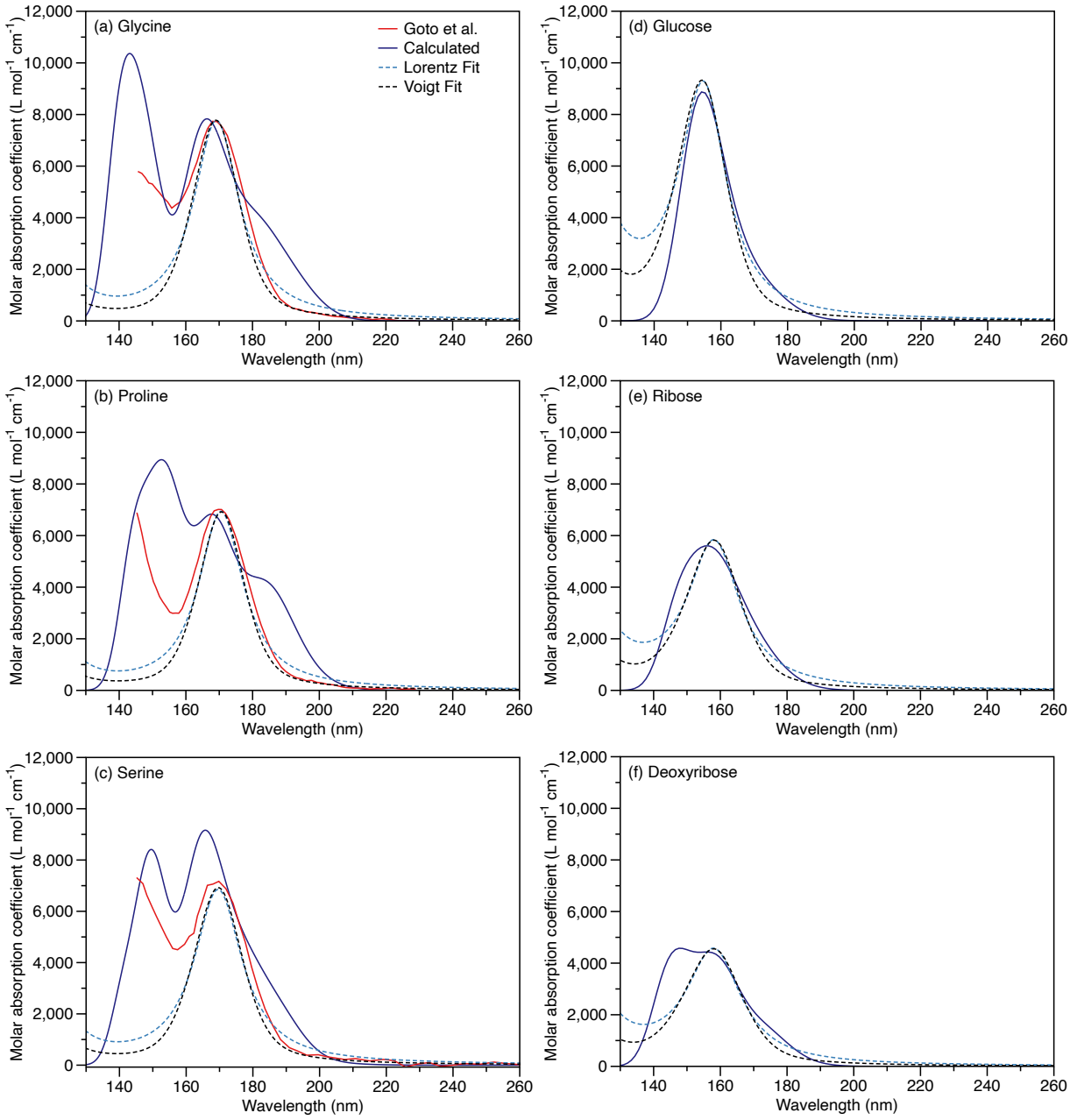

Figure S7: Far-UV molar absorptivity spectra for (a) glycine, (b) proline, (c) serine, (d) glucose, (e) ribose, and (f) deoxyribose. Red curves are experimental data from Ref. S17 (available only for the amino acids). Solid blue curves are TD-DFT results. Dashed blue curves are best-fits using a single Lorentzian function (Eq. S1) and dashed black curves are best-fits using a single Voigt function, with the fraction, f, fixed at 0.5 for all six solutes. The amino-acid fits use the experimental spectra,[S17] whereas the sugar fits use the calculated spectra. Fit parameters are listed in Table S3.

Table S3: Parameters used in the Lorentz and Voigt model of the microscopic polarizability for the organics studied here.

Species	α_∞ [$\times 10^{-40}$ SI]	α_1 [$\times 10^{-40}$ SI]	λ_1 (nm)	μ_1 (nm)
Glycine	7.72	5.17	169	1720
Proline	14.1	4.68	171	1800
Serine	10.9	4.63	170	1660
Glucose	18.5	4.88	155	1420
Ribose	15.0	3.30	159	1340
Deoxyribose	14.3	2.58	159	1260

7.2 Coupled-Dipole Theory and Calculations

Dipole–dipole coupling between molecules was calculated using equations as defined in Supporting Information of Ref. S8. The coupled-dipole equations describe the interactions of N electric dipoles within an embedding medium characterized by dielectric function ε_m. Each dipole, located at position $\mathbf{r}_i$, responds linearly to a local macroscopic electric field, $\mathbf{E}_i$, as described by its polarizability tensor $\boldsymbol{\alpha}_i$. The dipole moment $\mathbf{p}_i$ induced in each molecule is proportional to this field:

$$\mathbf{p}_i = \boldsymbol{\alpha}_i \mathbf{E}_i. \tag{S4}$$

In calculations here, we will consider both isotropic

$$\boldsymbol{\alpha}_i = \begin{pmatrix} \alpha_i & 0 & 0 \\ 0 & \alpha_i & 0 \\ 0 & 0 & \alpha_i \end{pmatrix} \tag{S5}$$

and unixaxial polarizability tensors

$$\boldsymbol{\alpha}_i = \begin{pmatrix} 0 & 0 & 0 \\ 0 & 0 & 0 \\ 0 & 0 & 3\alpha_i \end{pmatrix}, \tag{S6}$$

where α_i is the macroscopic polarizability of the ith dipole. To account for medium effects, the microscopic polarizability $\alpha_{\mathrm{micro},i}$ of the ith dipole is related to a macroscopic polarizability by

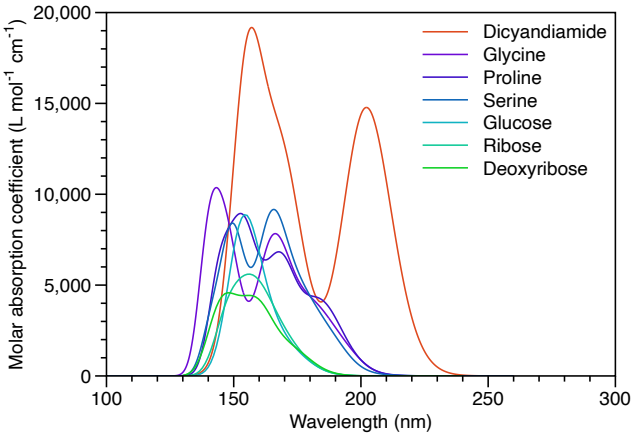

Figure S8: Far-UV molar absorptivity spectra calculated by TD-DFT for glycine, proline, serine, glucose, ribose, deoxyribose, and dicyandiamide. The more intense spectrum of dicyandiamide correlates with its rapid photochemistry.

incorporating a local-field correction factor L_m, as:

$$\alpha_i = L_m^2 \alpha_{\text{micro},i}, \tag{S7}$$

where $L_m = (\varepsilon_m + 2)/3$. Here, $\alpha_{\text{micro},i}$ will always be defined as α_d from Equation S1.

The resulting electric field at any position due to an individual dipole is given by a Green's tensor $\mathbf{G}(\mathbf{r}_i, \mathbf{r})$. Each dipole's effective field is the sum of the incident field and the scattered fields from other dipoles:

$$\mathbf{p}_i = \boldsymbol{\alpha}_i \left(\mathbf{E}_{\text{inc}}(\mathbf{r}_i) + \sum_{j \neq i}^{N} \mathbf{G}_{ij} \mathbf{p}_j \right), \tag{S8}$$

where $\mathbf{E}_{\text{inc}}$ is the incident electric field and the Green's tensor is

$$\mathbf{G}_{ij} = \frac{1}{\beta} \frac{e^{ik_m r_{ij}}}{r_{ij}} \left\{ k_m^2 [\mathbf{I} - \hat{\mathbf{r}}_{ij} \otimes \hat{\mathbf{r}}_{ij}] - \left(\frac{1}{r_{ij}^2} - \frac{ik_m}{r_{ij}} \right) [\mathbf{I} - 3\, \hat{\mathbf{r}}_{ij} \otimes \hat{\mathbf{r}}_{ij}] \right\}, \tag{S9}$$

where $\beta = 4\pi\varepsilon_0\varepsilon_m$, ε_0 is the vacuum permittivity, and k_m is the wavenumber in the embedding medium.

Here, the absorption cross-section, C_{abs}, for the system of N dipoles is calculated from the induced dipole moments and their local fields by:[S22]

$$C_{\text{abs}} = \frac{4\pi k_m}{\beta |E_0|^2} \sum_{i}^{N} \left(\text{Im}[\mathbf{p}_i \cdot \mathbf{E}_i^*] - \frac{2\beta}{3} k_m^3 |\mathbf{p}_i|^2 \right). \tag{S10}$$

The absorption cross-section per dipole is then $\sigma_{\text{abs}} = C_{\text{abs}}/N$.

In calculations shown in Figures S9, S10, and S11, ε_m was determined using the parameterization the four-term Sellmeier dispersion formula and constants for water from Ref. S23.

Figure S9 shows σ_{abs} calculations for dipole pairs using parameters for glycine, proline, and serine from Table S3. Both the isotropic and uniaxial polarizability models are used and the dipoles are placed in the head-to-tail configuration. This is expected to yield the largest enhancement in σ_{abs} and thus represents an upper bound for the possible increase in σ_{abs}. As the inter-dipole distance, r_{12}, decreases from an isolated dipole to 0.5 nm, σ_{abs} increases at wavelengths substantially longer than the resonance wavelength in the microscopic polarizability of the molecule. Although uniaxial polarizability yields greater absorption enhancement compared to isotropic polarizability, the overall magnitude of this coupling-induced enhancement remains relatively modest across all examined species.

Figure S10 presents σ_{abs} calculations for dipoles randomly positioned within a spherical volume. In the uniaxial case, the dipole orientations are also randomly distributed. The number of dipoles in each calculation is determined by the molar concentration. To prevent unphysical overlap, no two dipoles are positioned closer than the average spacing calculated from the cubic root of the inverse number density of the pure solute (0.416 nm for glycine, 0.516 nm for proline, and 0.465 nm for serine). For both uniaxial and isotropic polarizability models, σ_{abs} increases with increasing concentration, although the enhancement remains modest. Calculations were limited to spherical particles with radii up to 10 nm, as larger particles would require more than 10^4 dipoles at higher concentrations, which is computationally prohibitive due to memory constraints. Therefore, in the next section we consider changes to σ_{abs} using an effective medium model.

7.3 Effective Medium Theory and Calculations

Following the Supporting Information of Ref. S8, the effective medium expression based on the Clausius-Mossotti (CM) relation is

$$\varepsilon_{\text{eff}} = \frac{1+2\left(\bar{\alpha}_m + c_s \frac{\alpha_{\text{micro}}}{3\varepsilon_0}\right)}{1-\left(\bar{\alpha}_m + c_s \frac{\alpha_{\text{micro}}}{3\varepsilon_0}\right)}, \tag{S11}$$

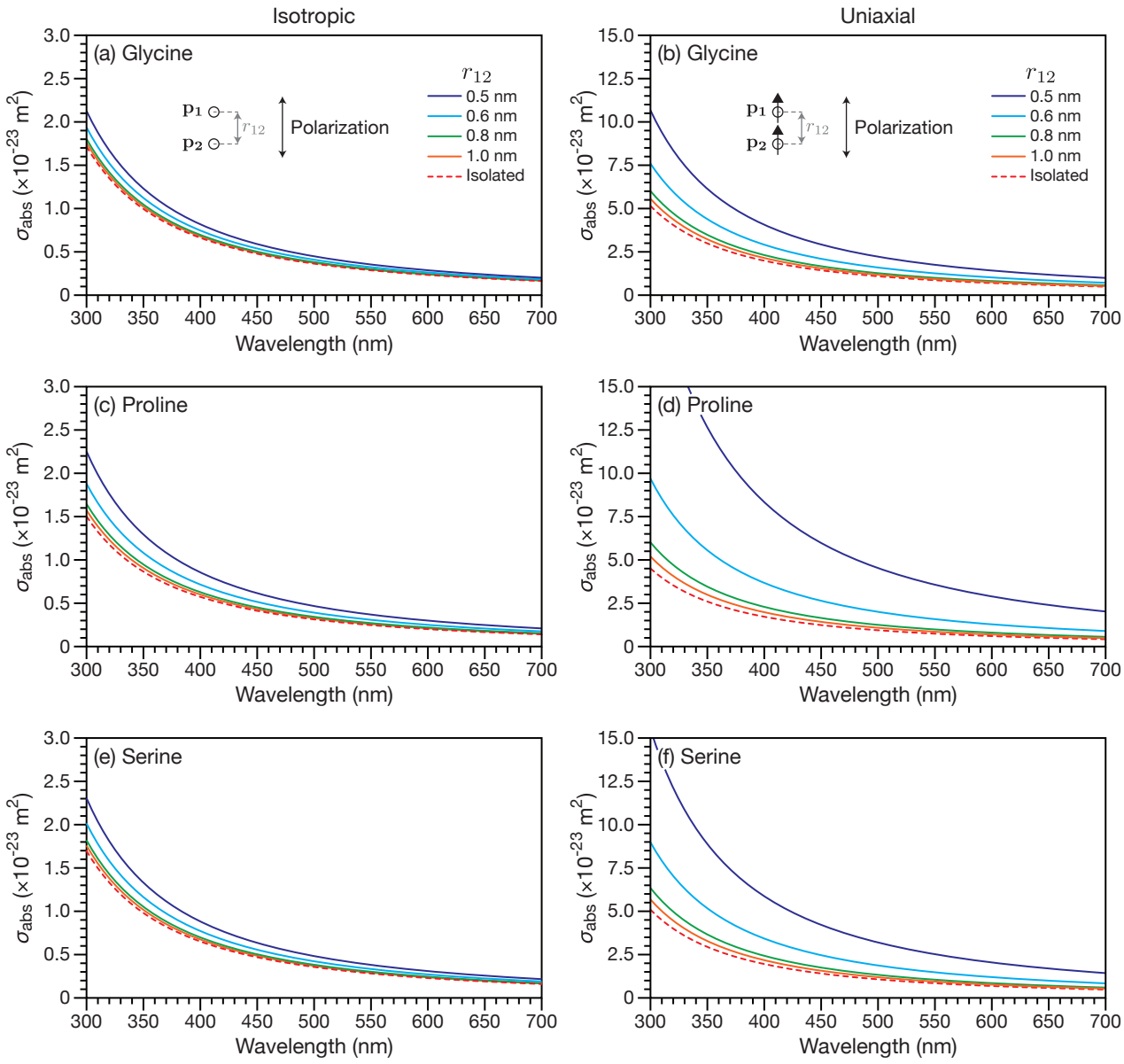

Figure S9: Absorption cross-section per dipole (σ_{abs}) calculated for a pair of dipoles separated by a distance r_{12}. Panels show results for (a,b) glycine, (c,d) proline, and (e,f) serine, using parameters listed in Table S3. Both isotropic (left column) and uniaxial (right column) cases are presented. In each case, the polarization of the incident light is aligned along the dipole axis. The dipoles are oriented in a head-to-tail configuration, which is expected to yield the largest enhancement in σ_{abs} at wavelengths much longer than the resonance wavelength in Equation S1. The dipoles are embedded in a medium with the refractive index of water.

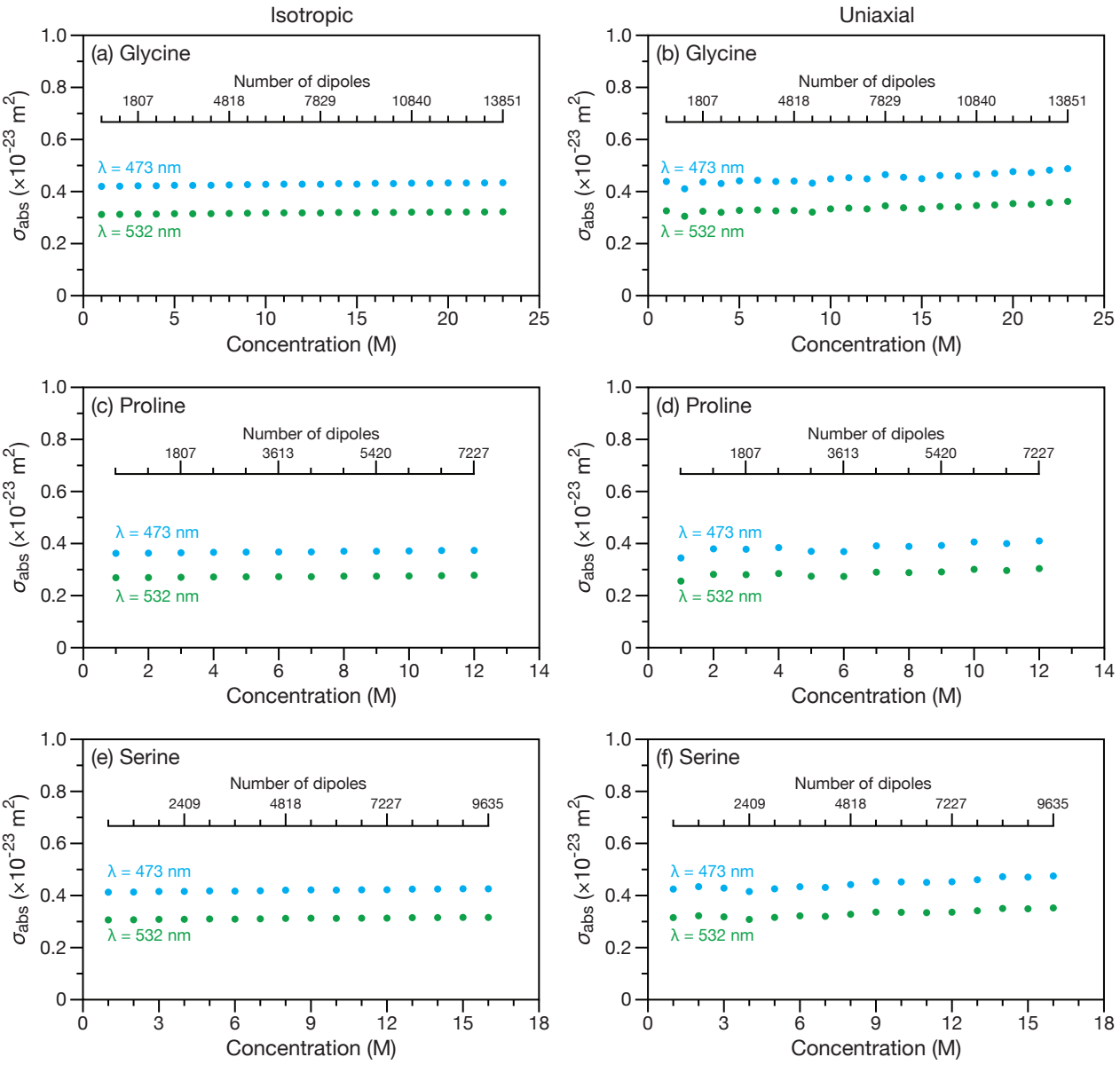

Figure S10: Absorption cross-section per dipole (σ_{abs}) calculated for randomly positioned dipoles contained within a 10 nm radius sphere with the number of dipoles set by the bulk concentration. Panels show results for (a,b) glycine, (c,d) proline, and (e,f) serine, using parameters listed in Table S3. Both isotropic (left column) and uniaxial (right column) cases are presented. In the uniaxial case, the dipole orientations are also randomly distributed.

where ε_{eff} is the effective relative permittivity of the composite medium, $\bar{\alpha}_m$ is the normalized polarizability of the solvent, α_{micro} is the microscopic polarizability defined earlier (here, it will be set to α_d from Equation S1), and c_s is the solute concentration. $\bar{\alpha}_m$ is determined using the CM relation applied to the pure solvent:

$$\bar{\alpha}_m = \frac{\varepsilon_m - 1}{\varepsilon_m + 2}. \tag{S12}$$

The complex refractive index of the composite medium is obtained directly from its effective permittivity,

$$m_{\text{eff}} = n_{\text{eff}} + ik_{\text{eff}} = \sqrt{\varepsilon_{\text{eff}}}, \tag{S13}$$

where

$$n_{\text{eff}} = \text{Re}(\sqrt{\varepsilon_{\text{eff}}}) \quad \text{and} \quad k_{\text{eff}} = \text{Im}(\sqrt{\varepsilon_{\text{eff}}}). \tag{S14}$$

The absorption coefficient of the effective medium is

$$\kappa_{\text{eff}} = \frac{4\pi}{\lambda} k_{\text{eff}}, \tag{S15}$$

which yields an absorption cross-section per molecule

$$\sigma_{\text{abs}} = \frac{\kappa_{\text{eff}}}{c_s}. \tag{S16}$$

Figure S11 shows σ_{abs} calculated using Equation S16 at the two experimental wavelength for glycine, proline, and serine using the parameters from Table S3. The maximum concentration for each species is based on the molar volumes of each solute.

If we now consider homogeneous spherical particles, the complex refractive index provided by the effective-medium expression (Equation S13) can be used directly in Mie-theory calculations[S24] of scattering and absorption cross-sections, allowing systematic exploration of both particle size and solute concentration.

The left column of Figure S12 presents the absorption cross-section, C_{abs}, computed with Mie theory for a sphere whose complex refractive index is determined by Equation S13 and the Lorentz parameters listed in Table S3. Calculations are shown at a single wavelength ($\lambda = 473$ nm) for several solute concentrations. The right column of Figure S12 divides each C_{abs} value by the total number of molecules in the corresponding sphere, yielding an effective

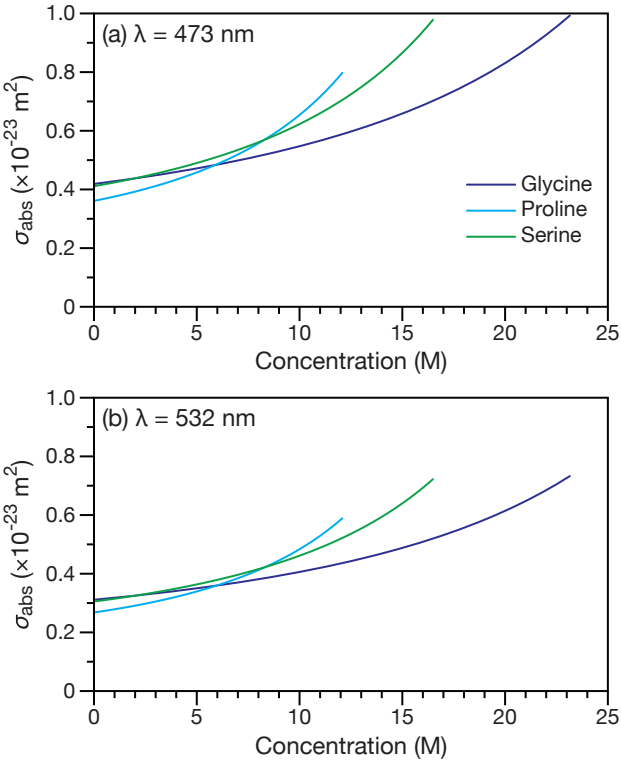

Figure S11: Absorption cross-section per molecule (σ_{abs}) of glycine, proline, and serine solutes in water calculated using effective medium theory (Equation S16) at the two experimental wavelengths: (a) 473 nm and (b) 532 nm. Parameters used are provided in Table S3. The maximum concentration shown for each solute is determined by its molar volume.

molecular absorption cross-section, σ_{abs}, in order to reveal any size- or concentration-dependent enhancement.

Between roughly radii of 0.1 and 1 μm, broad Mie resonances increase σ_{abs} at the higher solute concentrations. For radii between 1 and 10 μm, which are relevant to the experiments reported here, those increases at higher solute concentrations are absent. Instead, sharp peaks associate with Mie resonances appear at low concentrations (0.01 and 1 M) but are attenuated at higher concentrations due to the presence of more molecules. Overall, in this size range there is little difference in σ_{abs} at high solute concentrations. Therefore, Mie theory coupled with the effective-medium refractive index predicts little absorption enhancements for micron-sized particles for solute concentrations relevant to our experiments.

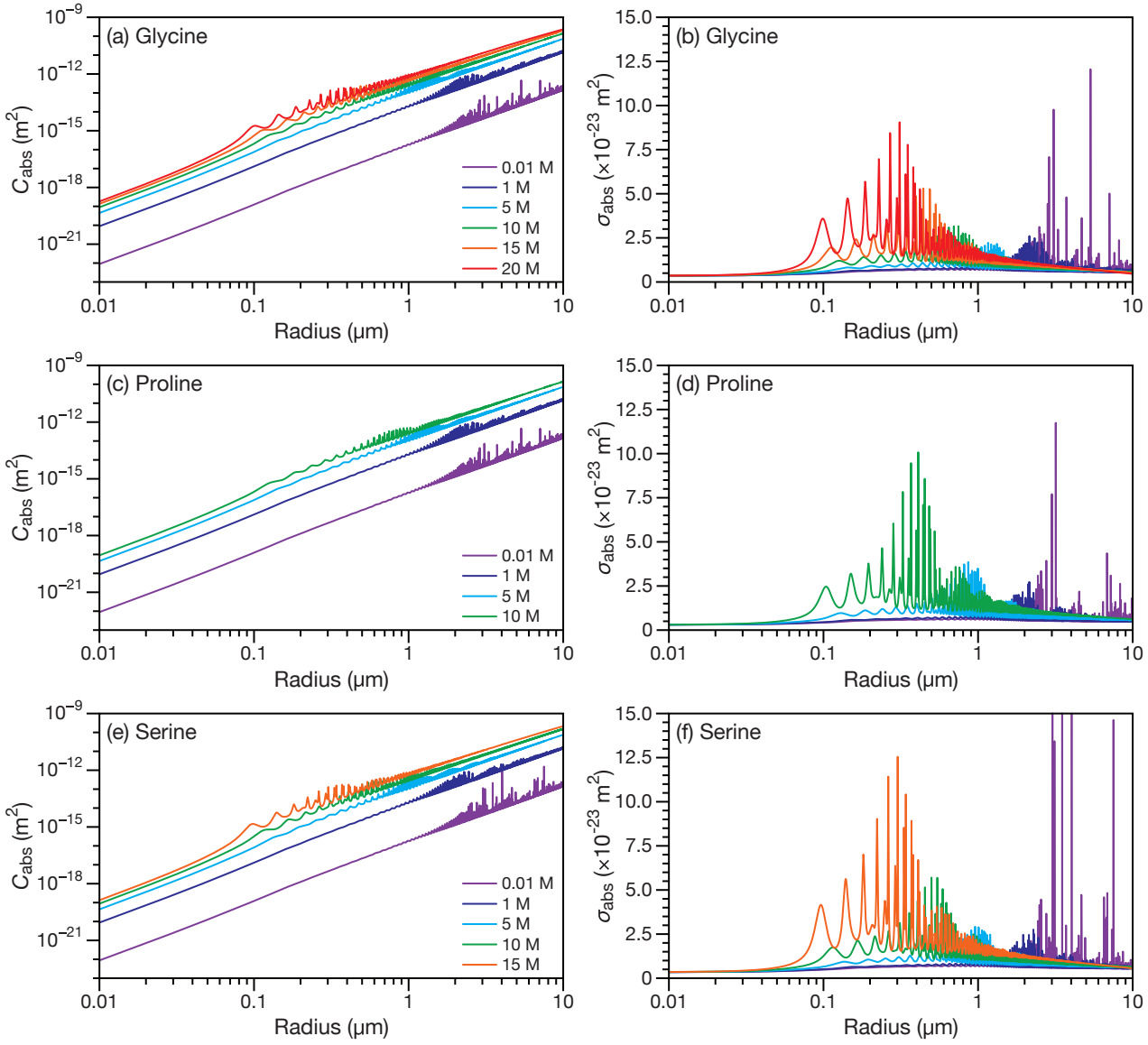

Figure S12: Absorption cross-section (C_{abs}, left column) and a corresponding absorption cross-section per molecule (σ_{abs}, right column) for a spherical particle calculated using full Mie theory with $\lambda = 473$ nm. Panels show results for (a,b) glycine, (c,d) proline, and (e,f) serine, using parameters listed in Table S3 and Equation S13. For panels (b), (d), and (f), the molecular absorption cross-section, σ_{abs}, is obtained by taking the corresponding C_{abs} value from panels (a), (c), and (e) and dividing it by the total number of molecules contained in the sphere with that radius and solute concentration.

8 Single–Molecule Absorption in a Dielectric Medium

The absorption cross-section of a single molecule embedded in a medium is[S8]

$$\sigma_{\text{abs}} = \frac{2\pi}{\lambda\varepsilon_0\sqrt{\varepsilon_m}} L_m^2 \,\text{Im}(\alpha_d). \tag{S17}$$

Using the definition of α_d from Equation S1 yields

$$\sigma_{\text{abs}} = \frac{2\pi}{\lambda\varepsilon_0\sqrt{\varepsilon_m}} L_m^2 \,\text{Im}\left[\frac{\alpha_1\lambda_1}{\mu_1}\left(\frac{1}{1-\frac{\lambda_1^2}{\lambda^2}-i\frac{\lambda_1^2}{\lambda\mu_1}}\right)\right]. \tag{S18}$$

When $\lambda \gg \lambda_1$, Equation S18 can be approximated as

$$\sigma_{\text{abs}} \approx \frac{2\pi}{\lambda\varepsilon_0\sqrt{\varepsilon_m}} L_m^2 \left(\frac{\alpha_1\lambda_1^3}{\mu_1^2\lambda}\right). \tag{S19}$$

Therefore, the cross-section ratio for two wavelengths λ_a and λ_b that satisfy $\lambda \gg \lambda_1$ is

$$\frac{\sigma_{\text{abs}}^{\lambda_a}}{\sigma_{\text{abs}}^{\lambda_b}} = \left(\frac{\lambda_b}{\lambda_a}\right)^2. \tag{S20}$$

9 Comparison of Approximate Geometric Optics With Exact Electromagnetic Solutions

In the photochemical model presented in the main text, approximate geometric optics expressions are used to determine the absorption cross-sections for weakly absorbing droplets. To assess their accuracy, we present comparisons between these geometric optics approximations and exact calculations using Mie theory[S24] and Generalized Lorenz-Mie Theory (GLMT).[S25,S26] We provide results for both the absorption cross-section (C_{abs}) and absorption efficiency (Q_{abs}), which are related by

$$C_{\text{abs}} = \pi r^2 Q_{\text{abs}}, \tag{S21}$$

where r is the particle radius.

In Figure S13, we plot C_{abs} and Q_{abs} for a weakly absorbing spherical particle illuminated by a plane wave with wavelength $\lambda = 473$ nm as functions of particle radius. Results from exact

Mie theory and a simplified geometric optics approximation are compared for three different imaginary refractive index values, k. The geometric optics expression used is

$$C_{\text{abs}} = \frac{16\pi^2}{3}\frac{kr^3}{\lambda}. \tag{S22}$$

In Figure S14, C_{abs} and Q_{abs} are calculated for the same particle parameters as in Figure S13, except that the illumination is now a Gaussian beam with a beam waist w_0. In all calculations, the sphere is centered at the focal point of the Gaussian beam, with $w_0 = 500$ nm. The geometric optics expression used is

$$C_{\text{abs}} = \frac{8\pi^2}{3}\left(1-e^{-\frac{2r^2}{w_0^2}}\right)\frac{w_0^2 kr}{\lambda}. \tag{S23}$$

For cases where $r > w_0$, Equation (S23) can be approximated as

$$C_{\text{abs}} = \frac{8\pi^2}{3}\frac{w_0^2 kr}{\lambda}. \tag{S24}$$

In Figure S15, C_{abs} and Q_{abs} are calculated using the same Gaussian beam as in Figure S14, except the particle now consists of a weakly absorbing shell surrounding a non-absorbing core. The core-shell particle is centered at the Gaussian beam's focal point, with $w_0 = 500$ nm. The shell thickness, δ, is fixed at 1 nm. The geometric optics expression for this configuration is

$$C_{\text{abs}} = \frac{8\pi^2}{3}\left(1-e^{-\frac{2r^2}{w_0^2}}\right)\frac{w_0^2 k(r^3-(r-\delta)^3)}{\lambda r^2}, \tag{S25}$$

where r is the outer radius of the core-shell particle (see inset in Figure S15b).

For the limit where $r \gg \delta$ and $r > w_0$, Equation S25 simplifies to

$$C_{\text{abs}} = 8\pi^2\frac{w_0^2 k\delta}{\lambda}. \tag{S26}$$

To summarize the results presented here within the context of the photochemical model presented in the main text: when the radius of a weakly absorbing droplet exceeds the beam waist, the simplified geometric optics formulas given in Equations S24 and S26 capture the size scaling accurately and agree reasonably well with exact electromagnetic solutions. Most importantly, their straightforward forms provide immediate physical insight into the role of particle parameters in droplet kinetics. Therefore, they are suitable for the photochemical kinetic modeling discussed in the main text.

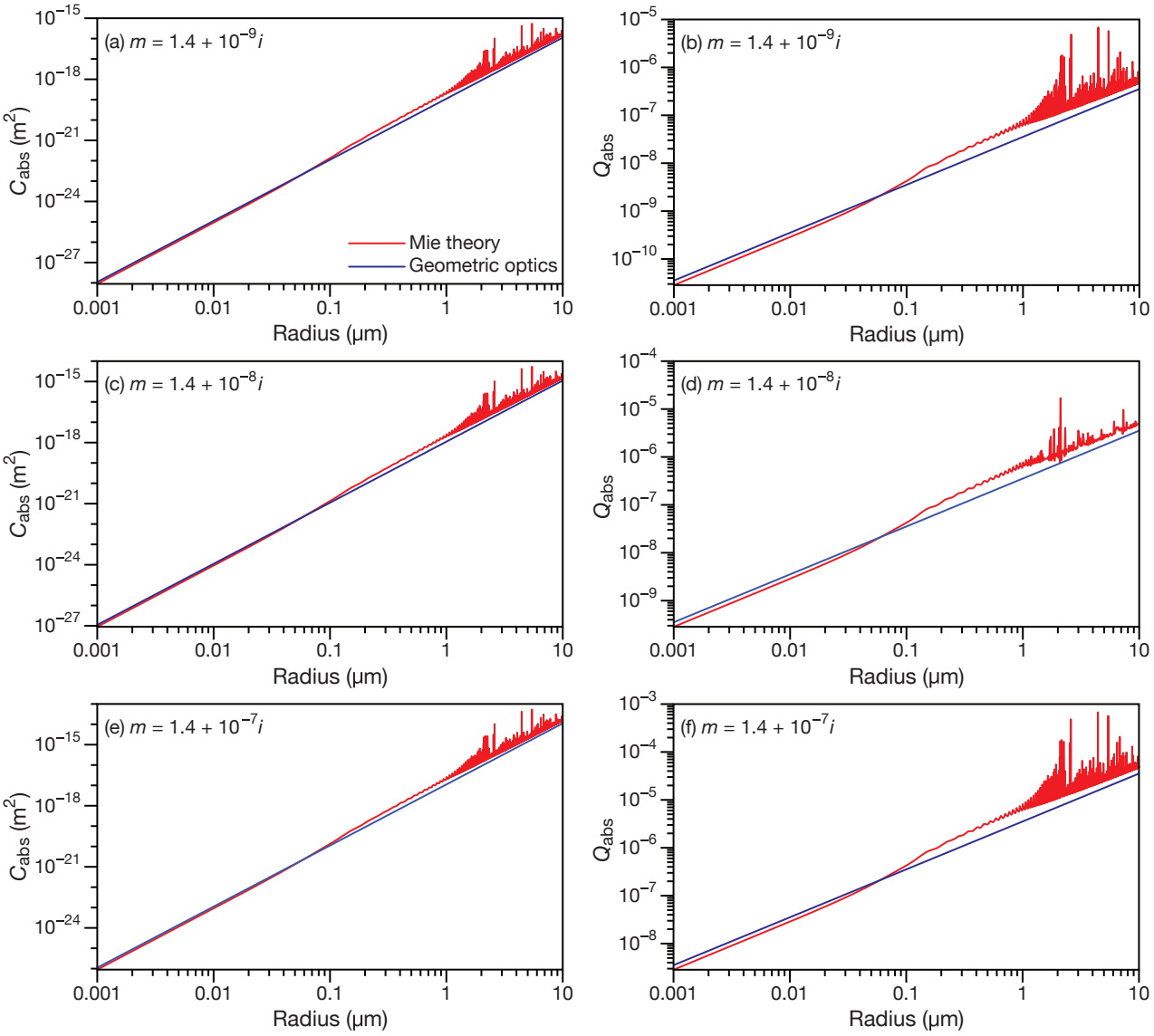

Figure S13: Absorption cross-section (C_{abs}, left column) and absorption efficiency (Q_{abs}, right column) for a spherical particle illuminated by an electromagnetic plane wave (λ = 473 nm) as functions of particle radius, calculated using full Mie theory (red lines) and a simplified geometric optics approximation (for C_{abs}, dark blue lines are calculated using Equation S22). The complex refractive index, m, has a real part of 1.4 and an imaginary part of (a, b) 10^{-9}, (c, d) 10^{-8}, and (e, f) 10^{-7}.

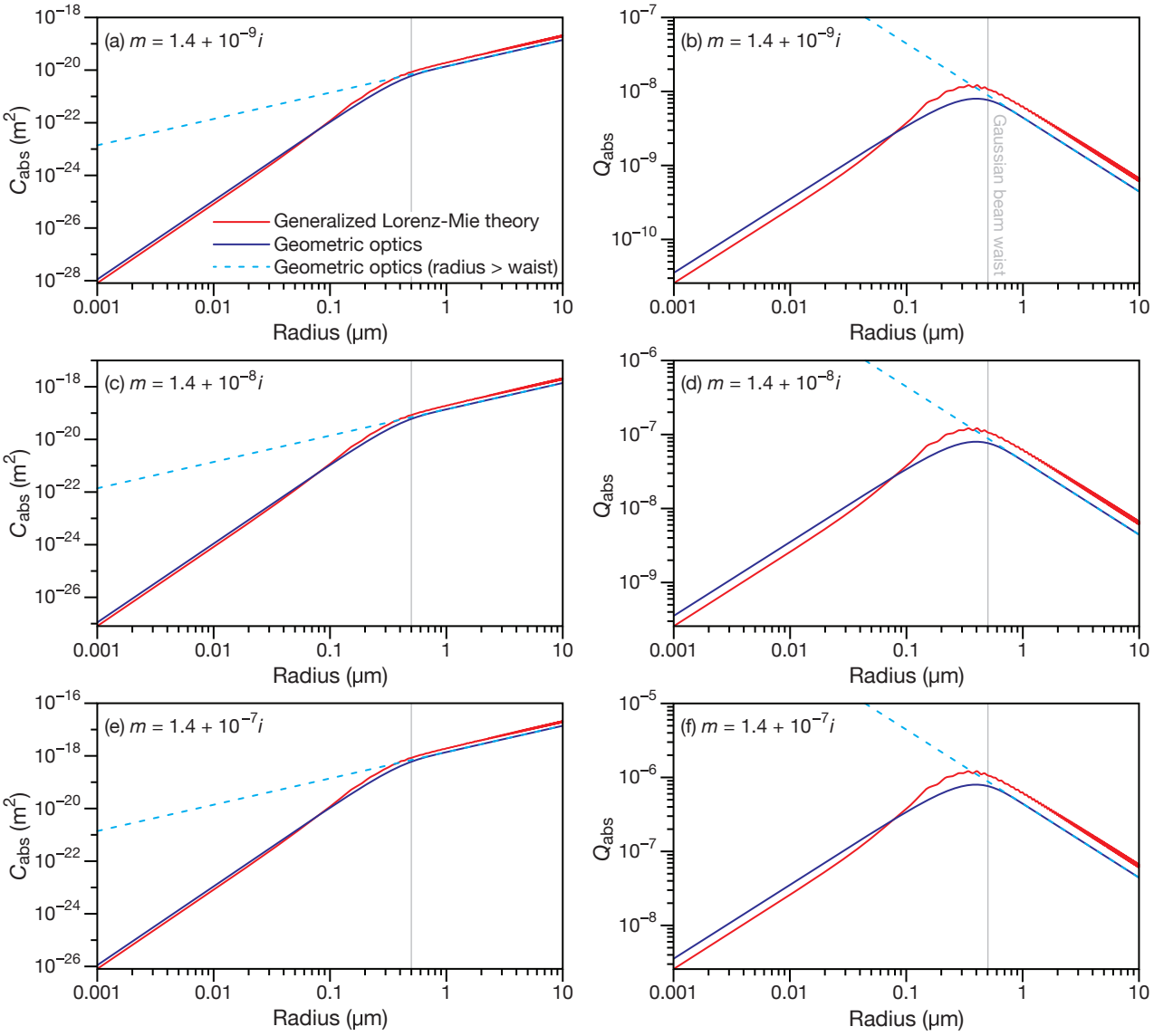

Figure S14: Absorption cross-section (C_{abs}, left column) and absorption efficiency (Q_{abs}, right column) for a spherical particle illuminated by a focused Gaussian beam ($\lambda = 473$ nm) as functions of particle radius, calculated using full Generalized Lorenz-Mie theory (red lines) and simplified geometric optics approximations (for C_{abs}, dark blue lines are calculated using Equation S23 and light blue dashed lines are calculated using Equation S24). The spherical particle is centered on the focal point of the beam and the beam waist is 500 nm. The complex refractive index, m, has a real part of 1.4 and an imaginary part of (a, b) 10^{-9}, (c, d) 10^{-8}, and (e, f) 10^{-7}.

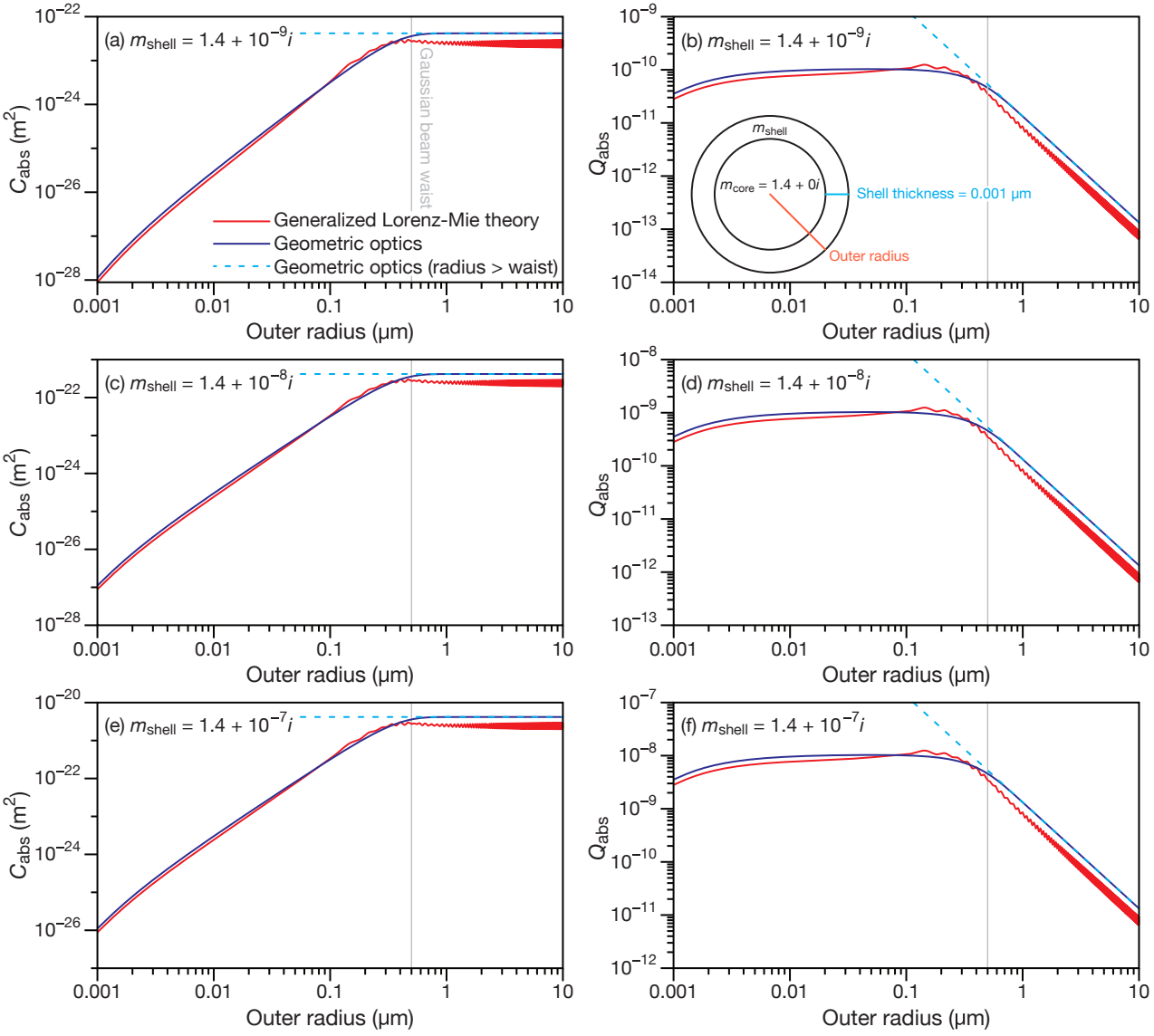

Figure S15: Absorption cross-section (C_{abs}, left column) and absorption efficiency (Q_{abs}, right column) for a spherical core-shell particle illuminated by a focused Gaussian beam ($\lambda = 473$ nm) as functions of outer particle radius, calculated using full Generalized Lorenz-Mie theory (red lines) and simplified geometric optics approximations (for C_{abs}, dark blue lines are calculated using Equation S25 and light blue dashed lines are calculated using Equation S26). The core-shell particle is centered on the focal point of the beam and the beam waist is 500 nm. The complex refractive index of the shell, m_{shell}, has a real part of 1.4 and an imaginary part of (a, b) 10^{-9}, (c, d) 10^{-8}, and (e, f) 10^{-7}. In all calculations, the shell thickness is always fixed at 1 nm and the complex refractive index of the core, m_{core}, is fixed with a real part of 1.4 and an imaginary part of zero.

References

[S1] Rumble, J. R. (ed.) *CRC Handbook of Chemistry and Physics* (CRC Press, 2024), 105 edn. URL `https://hbcp.chemnetbase.com`. Internet Version 2024. Last accessed 1 June 2025.

[S2] Gysel, M., Weingartner, E., Nyeki, S., Paulsen, D., Baltensperger, U., Galambos, I. & Kiss, G. Hygroscopic properties of water-soluble matter and humic-like organics in atmospheric fine aerosol. *Atmos. Chem. Phys.* **4**, 35–50 (2004).

[S3] Zuend, A., Marcolli, C., Luo, B. P. & Peter, T. A thermodynamic model of mixed organic-inorganic aerosols to predict activity coefficients. *Atmos. Chem. Phys.* **8**, 4559–4593 (2008).

[S4] Zuend, A., Marcolli, C., Booth, A. M., Lienhard, D. M., Soonsin, V., Krieger, U., Topping, D. O., McFiggans, G., Peter, T. & Seinfeld, J. H. New and extended parameterization of the thermodynamic model aiomfac: calculation of activity coefficients for organic-inorganic mixtures containing carboxyl, hydroxyl, carbonyl, ether, ester, alkenyl, alkyl, and aromatic functional groups. *Atmos. Chem. Phys.* **11**, 9155–9206 (2011).

[S5] Zeng, Z. *Hygroscopic Tandem Differential Mobility Analyzer (HTDMA) Design and Testing for Aerosol Hygroscopic Behavior Studies*. Ph.D. thesis, Bucknell University (2023).

[S6] Peng, C., Chow, A. H. & Chan, C. K. Hygroscopic study of glucose, citric acid, and sorbitol using an electrodynamic balance: Comparison with unifac predictions. *Aerosol Sci. Technol.* **35**, 753–758 (2001).

[S7] Miyawaki, O., Saito, A., Matsuo, T. & Nakamura, K. Activity and activity coefficient of water in aqueous solutions and their relationships with solution structure parameters. *Biosci. Biotechnol. Biochem.* **61**, 466–469 (1997).

[S8] Auguié, B. & Le Ru, E. C. Optical absorption of dye molecules in a spherical shell geometry. *J. Phys. Chem. C* **122**, 19110–19115 (2018).

[S9] Frisch, M. J., Trucks, G. W., Schlegel, H. B., Scuseria, G. E., Robb, M. A., Cheeseman, J. R., Scalmani, G., Barone, V., Petersson, G. A., Nakatsuji, H. *et al.* Gaussian˜16 Revision C.01 (2016). Gaussian Inc. Wallingford CT.

[S10] Dennington, R., Keith, T. A. & Millam, J. M. Gaussview Version 6 (2019). Semichem Inc. Shawnee Mission KS.

[S11] Adamo, C. & Barone, V. Toward reliable density functional methods without adjustable parameters: The PBE0 model. *J. Chem. Phys.* **110**, 6158–6170 (1999).

[S12] Weigend, F. & Ahlrichs, R. Balanced basis sets of split valence, triple zeta valence and quadruple zeta valence quality for h to rn: Design and assessment of accuracy. *Phys. Chem. Chem. Phys.* **7**, 3297–3305 (2005).

[S13] Weigend, F. Accurate coulomb-fitting basis sets for h to rn. *Phys. Chem. Chem. Phys.* **8**, 1057–1065 (2006).

[S14] Miertuš, S., Scrocco, E. & Tomasi, J. Electrostatic interaction of a solute with a continuum. a direct utilizaion of ab initio molecular potentials for the prevision of solvent effects. *Chem. Phys.* **55**, 117–129 (1981).

[S15] Cossi, M., Barone, V., Cammi, R. & Tomasi, J. Ab initio study of solvated molecules: a new implementation of the polarizable continuum model. *Chem. Phys. Lett.* **255**, 327–335 (1996).

[S16] Djorović, A., Meyer, M., Darby, B. L. & Le Ru, E. C. Accurate modeling of the polarizability of dyes for electromagnetic calculations. *ACS Omega* **2**, 1804–1811 (2017).

[S17] Goto, T., Ikehata, A., Morisawa, Y. & Ozaki, Y. Electronic transitions of protonated and deprotonated amino acids in aqueous solution in the region 145–300 nm studied by attenuated total reflection far-ultraviolet spectroscopy. *J. Phys. Chem. A* **117**, 2517–2528 (2013).

[S18] Yanai, T., Tew, D. P. & Handy, N. C. A new hybrid exchange–correlation functional using the coulomb-attenuating method (cam-b3lyp). *Chem. Phys. Lett.* **393**, 51–57 (2004).

[S19] Dunning Jr, T. H. Gaussian basis sets for use in correlated molecular calculations. i. the atoms boron through neon and hydrogen. *J. Chem. Phys.* **90**, 1007–1023 (1989).

[S20] Štěpánek, P. & Bouř, P. Multi-scale modeling of electronic spectra of three aromatic amino acids: Importance of conformational averaging and explicit solute–solvent interactions. *Phys. Chem. Chem. Phys.* **16**, 20639–20649 (2014).

[S21] Šebek, J., Kejík, Z. & Bouř, P. Geometry and solvent dependence of the electronic spectra of the amide group and consequences for peptide circular dichroism. *J. Phys. Chem. A* **110**, 4702–4711 (2006).

[S22] There is a typo where β is placed in the prefactor of Eq. S20 from Ref. S8. This is corrected in Eq. S10.

[S23] Daimon, M. & Masumura, A. Measurement of the refractive index of distilled water from the near-infrared region to the ultraviolet region. *Appl. Opt.* **46**, 3811–3820 (2007).

[S24] Bohren, C. F. & Huffman, D. R. *Absorption and scattering of light by small particles* (John Wiley & Sons, 2008).

[S25] Gouesbet, G., Lock, J. & Gréhan, G. Generalized Lorenz–Mie theories and description of electromagnetic arbitrary shaped beams: localized approximations and localized beam models, a review. *J. Quant. Spectrosc. Radiat. Transf.* **112**, 1–27 (2011).

[S26] Vennes, B. & Preston, T. C. Optical deformation of homogeneous and core-shell spherical particles. *Phys. Rev. A* **101**, 063812 (2020).